

Restless Tuneup of High-Fidelity Qubit Gates

M. A. Rol,^{1,2} C. C. Bultink,^{1,2} T. E. O'Brien,³ S. R. de Jong,^{1,2} L. S. Theis,⁴
X. Fu,¹ F. Luthi,^{1,2} R. F. L. Vermeulen,^{1,2} J. C. de Sterke,^{5,1} A. Bruno,^{1,2}
D. Deurloo,^{6,1} R. N. Schouten,^{1,2} F. K. Wilhelm,⁴ and L. DiCarlo^{1,2}

¹*QuTech, Delft University of Technology, P.O. Box 5046, 2600 GA Delft, The Netherlands*

²*Kavli Institute of Nanoscience, Delft University of Technology,
P.O. Box 5046, 2600 GA Delft, The Netherlands*

³*Instituut-Lorentz for Theoretical Physics, Leiden University, Leiden, The Netherlands*

⁴*Theoretical Physics, Saarland University, 66123 Saarbrücken, Germany*

⁵*Topic Embedded Systems B.V., P.O. Box 440, 5680 AK Best, The Netherlands*

⁶*Netherlands Organisation for Applied Scientific Research (TNO),
P.O. Box 155, 2600 AD Delft, The Netherlands*

(Dated: March 7, 2022)

We present a tuneup protocol for qubit gates with tenfold speedup over traditional methods reliant on qubit initialization by energy relaxation. This speedup is achieved by constructing a cost function for Nelder-Mead optimization from real-time correlation of non-demolition measurements interleaving gate operations without pause. Applying the protocol on a transmon qubit achieves 0.999 average Clifford fidelity in one minute, as independently verified using randomized benchmarking and gate set tomography. The adjustable sensitivity of the cost function allows detecting fractional changes in gate error with nearly constant signal-to-noise ratio. The restless concept demonstrated can be readily extended to the tuneup of two-qubit gates and measurement operations.

Reliable quantum computing requires the building blocks of algorithms, quantum gates, to be executed with low error. Strategies aiming at quantum supremacy without error correction [1, 2] require $\sim 10^3$ gates, and thus gate errors $\sim 10^{-3}$. Concurrently, a convincing demonstration of quantum fault tolerance using the circuits Surface-17 and -49 [3, 4] under development by several groups worldwide requires gate errors one order of magnitude below the $\sim 10^{-2}$ threshold of surface code [5, 6].

The quality of qubit gates depends on qubit coherence times and the accuracy and precision of the pulses realizing them. With the exception of a few systems known with metrological precision [7], pulsing requires meticulous calibration by closed-loop tuning, i.e., pulse adjustment based on experimental observations. Numerical optimization algorithms have been implemented to solve a wide range of tuning problems with a cost-effective number of iterations [8–13]. However, relatively little attention has been given to quantitatively exploring the speed and robustness of the algorithms used. This becomes crucial with more complex and precise quantum operations, as the number of parameters and requisite precision of calibration grow.

Though many aspects of tuning qubit gates are implementation independent, some details are specific to physical realizations. Superconducting transmon qubits are a promising hardware for quantum computing, with gate times already exceeding coherence times by three orders of magnitude. Conventional gate tuneup relies on qubit initialization, performed passively by waiting several times the qubit energy-relaxation time T_1 or actively through feedback-based reset [14]. Passive initialization becomes increasingly inefficient as T_1 steadily increases [15, 16], while feedback-based reset is technically involved [17].

In this Letter, we present a gate tuneup method that dispenses with T_1 initialization and achieves tenfold speedup over the state of the art [9] without active reset. Restless tuneup exploits the real-time correlation of quantum-non-demolition (QND) measurements interleaving gate operations without pause, and the evaluation of a cost function for numerical optimization with adjustable sensitivity at all levels of gate fidelity. This cost function is obtained from a simple modification of the gate sequences of conventional randomized benchmarking (CRB) to penalize both gate errors within the qubit subspace and leakage from it. We quantitatively match the signal to noise ratio of this cost function with a model that includes measured T_1 fluctuations. Restless tuneup robustly achieves T_1 -dominated gate fidelity of 0.999, verified using both CRB with T_1 initialization and a first implementation of gate set tomography (GST) in a superconducting qubit. While this performance matches that of conventional tuneup, restless is tenfold faster and converges in one minute.

In many tuneup routines [Fig. 1(a)], the relevant information from the measurements can be expressed as the fraction ε of non-ideal outcomes (m_n). In conventional gate tuneup, a qubit is repeatedly initialized in the ground state $|0\rangle$, driven by a set of gates ($\{G\}$) whose net operation is ideally identity, and measured [Fig. 1(b)]. The conventional cost function is the raw infidelity,

$$\varepsilon_C = \sum_{n=1}^N (m_n \neq 0) / N.$$

The central idea of restless tuning [Fig. 1(c)] is to remove the time-costly initialization step by measuring the correlation between subsequent QND measurements interleaving gate operations without any rest [18]. For ex-

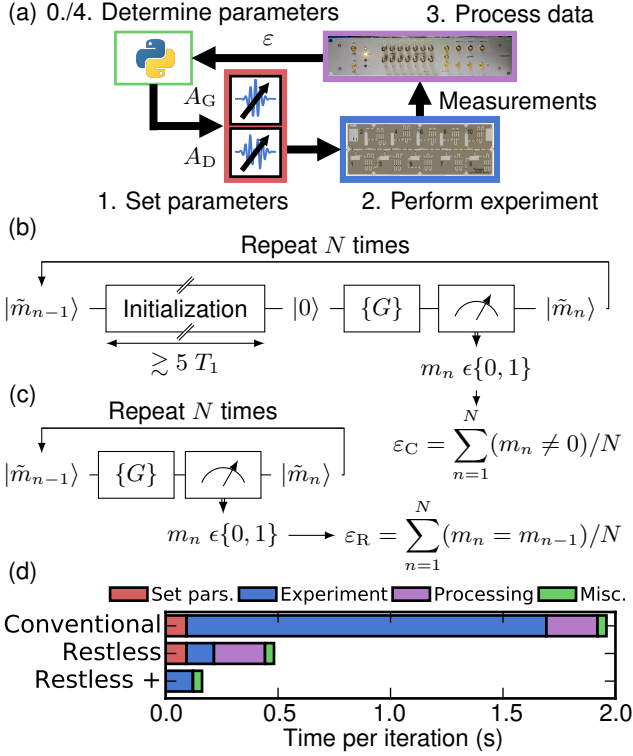


FIG. 1. (a) A general qubit gate tuneup loop. In conventional tuneup (b), the qubit is initialized before measuring the effect of $\{G\}$. In restless tuneup (c), the qubit is not initialized but m_{n-1} is used to estimate the initial state ($|\tilde{m}_{n-1}\rangle$). (d) Benchmark of various contributions to the time per iteration in conventional and restless tuneup, without and with technical improvements (see text for details).

ample, when the net ideal gate operation is a bit flip, we can define the error fraction

$$\epsilon_R = \sum_{n=2}^N (m_n = m_{n-1})/N. \quad (1)$$

We demonstrate restless tuneup of DRAG pulses [19] on the transmon qubit recently reported in [12]. We choose DRAG pulses (duration $\tau_p = 20$ ns) for their proven ability to reduce gate error and leakage [20, 21] with few-parameter analytic pulse shapes, consisting of Gaussian (G) and derivative of Gaussian (D) envelopes of the in- and quadrature-phase components of a microwave drive at the transition frequency f between qubit levels $|0\rangle$ and $|1\rangle$. These components are generated using four channels of an arbitrary waveform generator (AWG), frequency upconversion by sideband modulation of one microwave source, and two I-Q mixers. The G and D components are combined inside a vector switch matrix (VSM) [22] (details in [23]). A key advantage of this scheme using four channels is the ability to independently set the G and D amplitudes (A_G and A_D , respectively), without uploading new waveforms to the AWG.

To measure the speedup obtained from the restless method, we must take the complete iteration into ac-

count. The traditional iteration of a tuneup routine involves: (1) setting parameters (4 channel amplitudes on a Tektronix 5014 AWG); (2) acquiring $N = 8000$ measurement outcomes; (3) sending the measurement outcomes to the computer and processing them; and (4) miscellaneous overhead that includes determining the parameters for the next iteration, as well as saving and plotting data. In Fig. 1(d), we visualize these costs for an example optimization experiment. We intentionally penalize the restless method by choosing a large number of gates (~ 550). Even in these conditions, restless sequences reduce the acquisition time from 1.60 to 0.12 s. However, the improvement in total time per iteration (from 1.98 to 0.50 s) is modest due to 0.38 s of overhead.

We take two steps to reduce overhead. The 0.23 s required to send all measurement outcomes to the computer and then calculate the error fraction is reduced to < 1 ms by calculating the fraction in real time using the same FPGA system that digitizes and processes the raw measurement signals into bit outcomes. The 0.09 s required to set the four channel amplitudes in the AWG is reduced to 1 ms by setting A_G and A_D in the VSM. With these two technical improvements, the remaining overhead is dominated by the miscellaneous contributions (40 ms). This reduces the total time per restless (conventional) iteration to 0.16 s (1.64 s).

A quantity of common interest in gate tuneup is the average Clifford fidelity F_{Cl} , which is typically measured using CRB. In CRB, $\{G\}$ consists of sequences of N_{Cl} random Cliffords, including a final recovery Clifford that makes the ideal net operation identity. Following [24], we compose the 24 Cliffords from the set of π and $\pm\pi/2$ rotations around the x and y axes, which requires an average of 1.875 gates per Clifford. Gate errors make ϵ_C increase with N_{Cl} as [25, 26]

$$1 - \epsilon_C = A \cdot (p_{Cl})^{N_{Cl}} + B. \quad (2)$$

Here, A and B are constants determined by state preparation and measurement error (SPAM), and $1 - p_{Cl}$ is the average depolarizing probability per gate, making $F_{Cl} = \frac{1}{2} + \frac{1}{2}p_{Cl}$. Extracting F_{Cl} from a CRB experiment involves measuring ϵ_C for different N_{Cl} and fitting Eq. (2). However, for tuning it is sufficient to optimize ϵ_C at one choice of N_{Cl} , because $\epsilon_C(N_{Cl})$ decreases monotonically with F_{Cl} [9].

Due to leakage, CRB sequences and ϵ_C are not well suited for restless tuneup. Typically, there is significant overlap in readout signals for the first- ($|1\rangle$) and second- ($|2\rangle$) excited state of a transmon. A transmon in $|2\rangle$ can produce a string of identical measurement outcomes until it relaxes back to the qubit subspace. If the ideal net operation of $\{G\}$ is identity, the measurement outcomes can be indistinguishable from ideal behavior. By choosing the recovery Clifford for restless randomized benchmarking (RRB) sequences so that the ideal net operation of $\{G\}$ is a bit flip, we penalize leakage and make ϵ_R a suitable cost function.

We now examine the suitability of the restless scheme

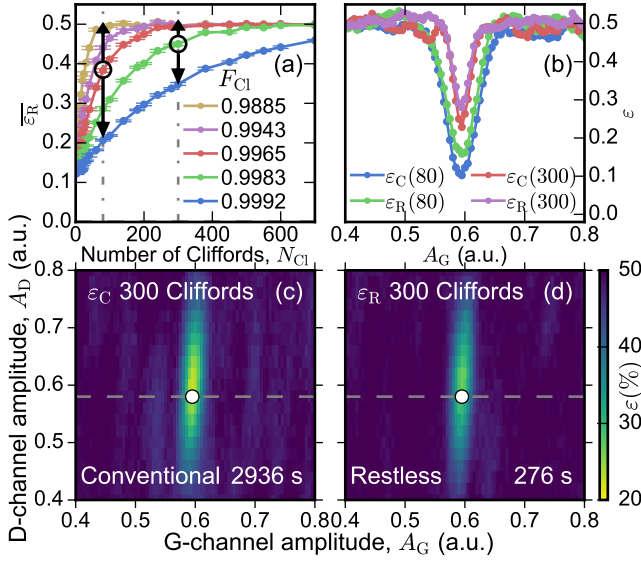


FIG. 2. (a) Average error fraction of RRB for different F_{CI} vs N_{CI} . (b) ε_C and ε_R as a function of A_G for $N_{CI} = 80$ and $N_{CI} = 300$. The curves are denoted by a dashed line in (c-d). (c-d) ε for $N_{CI} = 300$ as a function of A_G and A_D . White circles indicate minimal ε . Total acquisition time is shown at the bottom right.

for optimization (Fig. 2). Plots of the average $\varepsilon_R(N_{CI})$ [$\overline{\varepsilon}_R(N_{CI})$] at various F_{CI} (controlled via A_G) behave similarly to ε_C in CRB. Furthermore, ε_R is minimized at the same A_G as ε_C , with only a shallower dip because of SPAM. The (A_G, A_D) landscapes for both cost functions [Fig. 2(c-d)] are smooth around the optimum, making them suitable for numerical optimization. The fringes far from the optimum arise from the limited number of seeds (always 200) used to generate the RB sequences. Note that, while the landscapes are visually similar, the difference in time required to map them is striking, ~ 50 min for ε_C versus < 5 min for ε_R at $N_{CI} = 300$.

The sensitivity of ε_R to the tuning parameters depends on both the gate fidelity and N_{CI} . This can be seen in the variations between curves in Fig. 2(a). In order to quantify this sensitivity, we define a signal-to-noise ratio (SNR). For signal we take the average change in the error fraction, $\Delta\overline{\varepsilon}_R = \overline{\varepsilon}_R(F_{CI}^b) - \overline{\varepsilon}_R(F_{CI}^a)$, from F_{CI}^a to $F_{CI}^b \approx \frac{1}{2} + \frac{1}{2}F_{CI}^a$ (halving the infidelity). For noise we take $\overline{\sigma}_{\varepsilon_R}$, the average standard deviation of ε_R between F_{CI}^a and F_{CI}^b . We find that the maximal SNR remains ~ 15 for an optimal choice of N_{CI} that increases with F_{CI}^a (Fig. 3 and details in [23]). This allows tuning in logarithmic time since reducing error rates $p \rightarrow p/2^M$ requires only M optimization steps.

A simple model describes the measurement outcomes as independent and binomially distributed with error probability ε_R , as per Eq. (2) with $\varepsilon_C \rightarrow \varepsilon_R$. This model captures all the essential features of the signal. However, it only quantitatively matches the noise at high N_{CI} . Experiment shows an increase in noise at low N_{CI} . In this

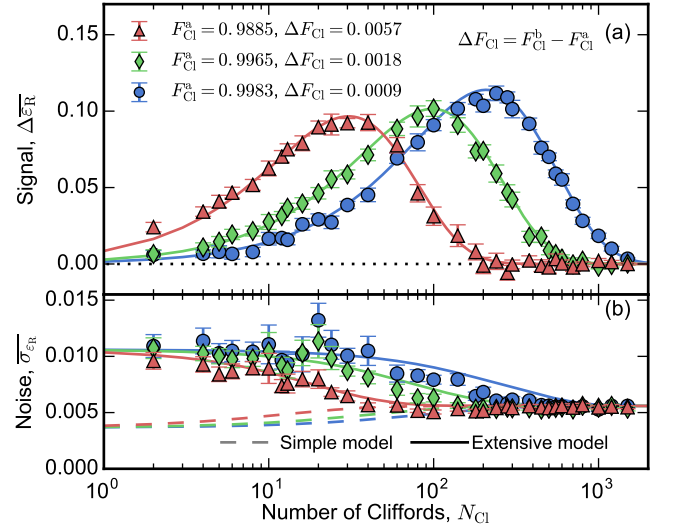


FIG. 3. (a) Signal $\Delta\overline{\varepsilon}_R$ for a halving of the gate infidelity, plotted as a function N_{CI} at $F_{CI}^a \sim 0.989$ (red), 0.996 (green) and 0.998 (blue). (b) Noise dependence on N_{CI} at the same fidelity levels. Added curves are obtained from the two models described in the main text.

range, ε_R is dominated by SPAM, which is primarily due to T_1 . We surmise that the increase stems from T_1 fluctuations [27] during the acquisition of statistics in these RRB experiments. To test this hypothesis, we develop an extensive model incorporating T_1 fluctuations into the calculation of both signal and noise [23]. We find good agreement with experimental results using independently measured values of T_1 and σ_{T_1} .

Following its validation, we now employ ε_R in a two-step numerical optimization protocol (Fig. 4). We choose the Nelder-Mead algorithm [28] as it is derivative-free and easy to use, requiring only the specification of a starting point and initial stepsizes. The first step using $\varepsilon_R(N_{CI} = 80)$ ensures convergence even when starting relatively far from the optimum, while the second step using $\varepsilon_R(N_{CI} = 300)$ fine tunes the result. We test the optimization for four realistic starting deviations from the optimal parameters ($A_D^{\text{opt}}, A_G^{\text{opt}}$). A_G starts at roughly 6% above or below A_G^{opt} , chosen as a worst-case estimate from a Rabi-oscillation experiment. A_D starts at roughly half or double A_D^{opt} . The initial stepsizes are $\Delta A_G \approx -0.03A_G^{\text{opt}}$, $\Delta A_D \approx -0.25A_D^{\text{opt}}$ for the first step, and $\Delta A_G \approx -0.01A_G^{\text{opt}}$, $\Delta A_D \approx -0.08A_D^{\text{opt}}$ for the second step.

We assess the accuracy of the above optimization and compare to traditional methods. A CRB experiment [Fig. 4(c)] following two-parameter restless optimization indicates $F_{CI} = 0.9991$. This value matches the average achieved by both restless and conventional tuneups for the different starting conditions. We also implement GST to independently verify results obtained using CRB. From the process matrices we extract the average GST Clifford fidelity, $F_{CI}^{\text{GST}} = 0.99907 \pm 0.00003$ ($0.99909 \pm$

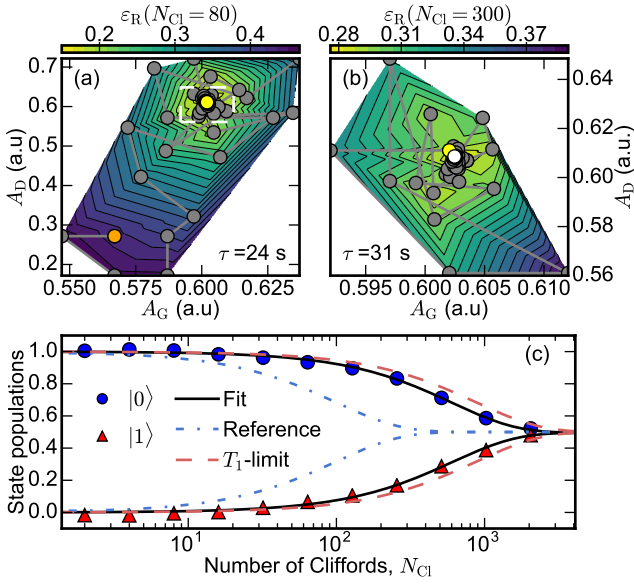


FIG. 4. Two-parameter restless tuneup using a two-step optimization, first at $N_{Cl} = 80$ (a) and then at $N_{Cl} = 300$ (b). Contour plots show a linear interpolation of ε_R . The starting point, intermediate result and final result are marked by orange, yellow and white dots, respectively. (c) CRB of tuned pulses ($F_{Cl} = 0.9991$), and compared to $F_{Cl}^{(T_1)} = 0.9994$ and $F_{Cl} = 0.995$ for reference.

	2-par. (A_G, A_D)		3-par. (A_G, A_D, f)	
	conv.	restl.	conv.	restl.
$\overline{F_{Cl}}$	0.9991	0.9991	0.9990	0.9990
$\sigma_{F_{Cl}}$	$3 \cdot 10^{-5}$	$3 \cdot 10^{-5}$	0.0001	0.0001
$\overline{\tau}$	660 s	59 s	610 s	66 s
σ_τ	110 s	11 s	110 s	13 s
$\overline{N_{it}}$	400	370	370	420
$\sigma_{N_{it}}$	70	70	70	80
$F_{Cl}^{(T_1)}$	0.9994		0.9993	
$\overline{T_1}$	21.4 μs		19.3 μs	

TABLE I. Tuning protocol performance. Mean (overlined) and standard deviations (denoted by σ) of F_{Cl} , time to convergence τ , and number of iterations N_{it} for restless and conventional tuneups with 2 and 3 parameters. Average T_1 measured throughout these runs and corresponding average $F_{Cl}^{(T_1)}$ are also listed.

0.00003) for restless (conventional) tuneup [23], consistent with the value obtained from CRB.

The robustness of the optimization protocol is tested by interleaving tuneups with CRB and T_1 measurements over 11 hours (summarized in Table I, and detailed in [23]). Both tuneups reliably converge to $F_{Cl} = 0.9991$,

close to the T_1 limit [29]:

$$F_{Cl}^{(T_1)} \approx \frac{1}{6} \left(3 + 2e^{-\tau_c/2T_1} + e^{-\tau_c/T_1} \right) = 0.9994, \quad (3)$$

with $\tau_c = 1.875 \tau_p$. However, restless tuneup converges in one minute while conventional tuneup requires eleven.

It remains to test how restless tuneup behaves as additional parameters are introduced. Many realistic scenarios also require tuning the drive frequency f . As a worst case, we take an initial detuning of ± 250 kHz. The initial stepsize in the first (second) step is 100 kHz (50 kHz). The 3-parameter optimization converges to $F_{Cl} = 0.9990 \pm 0.0001$ for both restless and conventional tuneups. We attribute the slight decrease in F_{Cl} achieved by 3-parameter optimization to the observed reduction in average T_1 .

In summary, we have developed an accurate and robust tuneup method achieving a tenfold speedup over the state of the art [9]. This speedup is achieved by avoiding qubit initialization by relaxation and using real-time correlation of measurement outcomes to build the cost function for numerical optimization. We have applied the restless concept to the tuneup of Clifford gates on a transmon qubit, reaching a T_1 -dominated fidelity of 0.999 in one minute, verified by conventional randomized benchmarking and gate set tomography. We have shown experimentally that the method can detect fractional reductions in gate error with nearly constant signal-to-noise ratio. Immediate next experiments will extend the restless concept to the tuneup of two-qubit gates and measurement operations, and to simultaneous tuneup of the physical qubits comprising a logical qubit.

ACKNOWLEDGMENTS

We thank R. Sagastizabal for experimental assistance, C. Dickel, J. Helsen, and S. Poletto for discussions, A. Johnson for support with Microsoft QCoDeS and K. Ruddinger, E. Nielsen and R. Blume-Kohout for support with GST/pyGSTi. This research is supported by the Office of the Director of National Intelligence (ODNI), Intelligence Advanced Research Projects Activity (IARPA), via the U.S. Army Research Office grant W911NF-16-1-0071. Additional funding provided by the ERC Synergy Grant QC-lab, the China Scholarship Council (X.F.) and Microsoft Corporation Station Q. The views and conclusions contained herein are those of the authors and should not be interpreted as necessarily representing the official policies or endorsements, either expressed or implied, of the ODNI, IARPA, or the U.S. Government. The U.S. Government is authorized to reproduce and distribute reprints for Governmental purposes notwithstanding any copyright annotation thereon.

- [2] P.-L. Dallaire-Demers and F. K. Wilhelm, arXiv:1606.00208 (2016).
- [3] C. Horsman, A. G. Fowler, S. Devitt, and R. V. Meter, New J. Phys. **14**, 123011 (2012).
- [4] Y. Tomita and K. M. Svore, Phys. Rev. A **90**, 062320 (2014).
- [5] A. G. Fowler, M. Mariantoni, J. M. Martinis, and A. N. Cleland, Phys. Rev. A **86**, 032324 (2012).
- [6] J. M. Martinis, npj Quantum Inf. **1**, 15005 (2015).
- [7] B. E. Anderson, H. Sosa-Martinez, C. A. Riofrío, I. H. Deutsch, and P. S. Jessen, Phys. Rev. Lett. **114**, 1 (2015).
- [8] D. J. Egger and F. K. Wilhelm, Phys. Rev. Lett. **112**, 1 (2014).
- [9] J. Kelly, R. Barends, B. Campbell, Y. Chen, Z. Chen, B. Chiaro, A. Dunsworth, A. G. Fowler, I.-C. Hoi, E. Jeffrey, A. Megrant, J. Mutus, C. Neill, P. J. J. O'Malley, C. Quintana, P. Roushan, D. Sank, A. Vainsencher, J. Wenner, T. C. White, A. N. Cleland, and J. M. Martinis, Phys. Rev. Lett. **112**, 240504 (2014).
- [10] J. Kelly, R. Barends, A. G. Fowler, A. Megrant, E. Jeffrey, T. C. White, D. Sank, J. Y. Mutus, B. Campbell, Y. Chen, Z. Chen, B. Chiaro, A. Dunsworth, E. Lucero, M. Neeley, C. Neill, P. J. J. O'Malley, C. Quintana, P. Roushan, A. Vainsencher, J. Wenner, and J. M. Martinis, Phys. Rev. A **94**, 032321 (2016).
- [11] D. T. McClure, H. Paik, L. S. Bishop, M. Steffen, J. M. Chow, and J. M. Gambetta, Phys. Rev. Appl. **5**, 011001 (2016).
- [12] C. C. Bultink, M. A. Rol, T. E. O'Brien, X. Fu, B. C. S. Dikken, C. Dickel, R. F. L. Vermeulen, J. C. de Sterke, A. Bruno, R. N. Schouten, and L. DiCarlo, Phys. Rev. Appl. **6**, 034008 (2016).
- [13] P. Cerfontaine, T. Botzem, S. S. Humpohl, D. Schuh, D. Bougeard, and H. Bluhm, arXiv:1606.01897 (2016).
- [14] D. Ristè, C. C. Bultink, K. W. Lehnert, and L. DiCarlo, Phys. Rev. Lett. **109**, 240502 (2012).
- [15] M. H. Devoret and R. J. Schoelkopf, Science **339**, 1169 (2013).
- [16] C. Wang, C. Axline, Y. Y. Gao, T. Brecht, Y. Chu, L. Frunzio, M. H. Devoret, and R. J. Schoelkopf, Appl. Phys. Lett. **107**, 162601 (2015).
- [17] D. Ristè and L. DiCarlo, ArXiv:1508.01385 (2015).
- [18] Except $3.25 \mu\text{s}$ needed for passive depletion of photons leftover from the $1 \mu\text{s}$ measurement [12].
- [19] F. Motzoi, J. M. Gambetta, P. Rebentrost, and F. K. Wilhelm, Phys. Rev. Lett. **103**, 110501 (2009).
- [20] J. M. Chow, L. DiCarlo, J. M. Gambetta, F. Motzoi, L. Frunzio, S. M. Girvin, and R. J. Schoelkopf, Phys. Rev. A **82**, 040305 (2010).
- [21] Z. Chen, J. Kelly, C. Quintana, R. Barends, B. Campbell, Y. Chen, B. Chiaro, A. Dunsworth, A. G. Fowler, E. Lucero, E. Jeffrey, A. Megrant, J. Mutus, M. Neeley, C. Neill, P. J. J. O'Malley, P. Roushan, D. Sank, A. Vainsencher, J. Wenner, T. C. White, A. N. Korotkov, and J. M. Martinis, Phys. Rev. Lett. **116**, 020501 (2016).
- [22] S. Asaad, C. Dickel, S. Poletto, A. Bruno, N. K. Langford, M. A. Rol, D. Deurloo, and L. DiCarlo, npj Quantum Inf. **2**, 16029 (2016).
- [23] See supplemental material at [insert URL] for additional data.
- [24] J. M. Epstein, A. W. Cross, E. Magesan, and J. M. Gambetta, Phys. Rev. A **89**, 062321 (2014).
- [25] E. Magesan, J. M. Gambetta, and J. Emerson, Phys. Rev. Lett. **106**, 180504 (2011).
- [26] E. Magesan, J. M. Gambetta, and J. Emerson, Phys. Rev. A **85**, 042311 (2012).
- [27] C. Müller, J. Lisenfeld, A. Shnirman, and S. Poletto, Phys. Rev. B **92**, 035442 (2015).
- [28] J. A. Nelder and R. Mead, The Computer Journal **7**, 308 (1965).
- [29] E. Magesan, private communication.

SUPPLEMENTAL MATERIAL FOR “RESTLESS TUNEUP OF HIGH-FIDELITY QUBIT GATES”

This supplement presents the hardware configuration used for the numerical tuneup, the characterization and modeling of the signal and noise of restless randomized benchmarking, and the procedure for calculating Clifford gate fidelities from GST process matrices. Finally, it presents the data summarized in Table 1 of the main text.

I. SETUP FOR NUMERICAL OPTIMIZATION

The key hardware components executing the tuneup loop of Fig. 1(a) are shown in Fig. S1. The computer is responsible for preparing the experiment and executing the numerical algorithm determining the parameter values for each iteration. To do this, the computer relies on two python packages, *PycQED* for cQED-specific routines [S1] and *QCoDeS* for the framework of instrument drivers [S2]. Part of the preparation consists of generating and uploading a sequence of control pulses and markers to the AWG. Once an experiment starts, the AWG is responsible for all time-critical matters, including gating the readout pulses on the microwave source and triggering the data acquisition on the FPGA controller. The control pulses are generated using 4 AWG channels, 2 for the I and Q quadratures of the Gaussian component and 2 for the quadratures of the derivative component. The components are upconverted using single-sideband mixers and a constant microwave tone as a local oscillator (LO). This allows independent control over the amplitude of both pulse components, using either the AWG or the VSM. The frequency of the pulses can be changed by changing the frequency of the LO. Note that all these controls can be applied without regenerating and uploading the sequence of control pulses to the AWG. The transmon is read-out by interrogating its dispersively coupled resonator near its fundamental frequency using a capacitively coupled feedline. Readout transients are amplified at the front end of the amplification chain by a Josephson parametric amplifier operated in the non-degenerate mode, providing 14 dB of gain. The FPGA controller performs final demodulation, integration and discrimination of measurement transients and real-time calculation of ε .

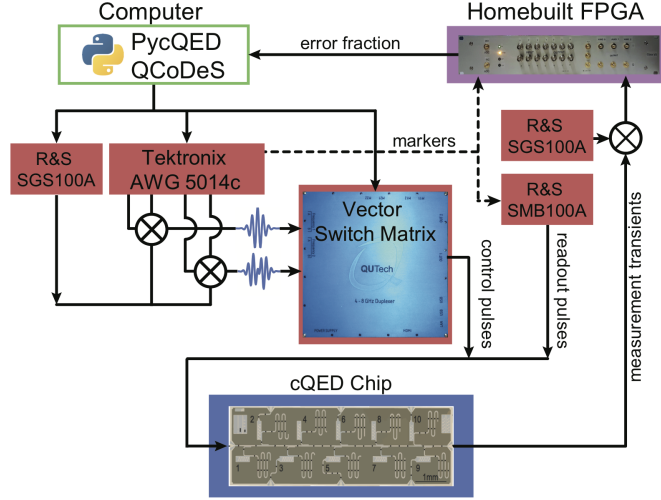


FIG. S1. Schematic overview of the hardware components used in the numerical tuneup.

II. SIGNAL AND NOISE OF THE RESTLESS COST FUNCTION

We experimentally obtained the signal and noise of RRB presented in Fig. 3 of the main text from 50 RRB experiments ($N = 8000$ measurement outcomes each) at each N_{C1} (32 values) and F_{C1} (5 values). Here, F_{C1} was varied by changing A_G . The procedure was repeated 10 times for all settings to build up statistics. In this section, we present the derivation of the extended model used to predict these curves (Section II A), using independent measurements of qubit T_1 fluctuations performed one day apart (Section II B).

A. Modelling

We develop a model for the RRB experiment to capture both the signal and noise obtained experimentally. The standard deviation differs from that simply expected from a binomial distribution. This is hypothesized to be caused by T_1 fluctuations that are quasi-static during individual RRB experiments but dynamic on the time scale required for 50 repetitions. We attempt to match the experimental results with a model containing T_1 and its fluctuations, a relaxation independent pulse error p_{pulse} , and a SPAM offset $p_s^{(c)}$. Independent measurements of the average and standard deviation of T_1 , and extractions of p_{pulse} and $p_s^{(c)}$ from the data in Fig. 2(a) are used to produce the model curves in Fig. 3.

1. Modeling without T_1 fluctuations

The time taken for a single-shot RRB experiment can be written $\tau_{\text{RRB}} = \tau_{\text{RO}} + \tau_{\text{Cl}} N_{\text{Cl}}$. The static time $\tau_{\text{RO}} = 4.25 \mu\text{s}$ is the readout-and-depletion time, whilst the Clifford-dependent time $\tau_{\text{Cl}} = 37.5 \text{ ns}$ is the average time it takes to perform a Clifford gate. To each of these we can associate an error rate, making the total error rate per single-shot experiment

$$p_e = p_s +_p N_{\text{Cl}} \times_p p_c.$$

Here, p_s is the error contribution due to SPAM, and $p_c = 1 - F_{\text{Cl}}$ is the error contribution per Clifford. We must be careful with adding probabilities here, as two errors cancel. This is taken care of by the probabilistic addition $a +_p b = a + b - 2ab = a(1 - b) + b(1 - a)$, and the probabilistic multiplication $c \times_p a = a +_p a +_p \dots +_p a$ (repeated c times for c a positive integer). This multiplication can be simplified:

$$\begin{aligned} N_{\text{Cl}} \times_p p_c &= N_{\text{Cl}} p_c (1 - p_c)^{N_{\text{Cl}}-1} + \binom{N_{\text{Cl}}}{3} p_c^3 (1 - p_c)^{N_{\text{Cl}}-3} + \dots \\ &= \frac{1}{2} [((1 - p_c) + p_c)^{N_{\text{Cl}}} - ((1 - p_c) - p_c)^{N_{\text{Cl}}}] \\ &= \frac{1}{2} [1 - (1 - 2p_c)^{N_{\text{Cl}}}], \end{aligned}$$

resulting in a final error rate

$$p_e = p_s + \frac{1}{2} [1 - (1 - 2p_c)^{N_{\text{Cl}}}] (1 - 2p_s). \quad (\text{S1})$$

2. Modelling with T_1 fluctuations

If p_s or p_c fluctuate, the error rate p_e for any given single-shot experiment is drawn from a distribution with mean

$$\overline{p_e} = \overline{p_s} + \frac{1}{2} [1 - (1 - 2\overline{p_c})^{N_{\text{Cl}}}] (1 - 2\overline{p_s}),$$

and variance

$$\begin{aligned} \text{var}(p_e) &= (1 - 2\overline{p_c})^{2N_{\text{Cl}}} \text{var}(p_s) + N_{\text{Cl}}^2 (1 - 2\overline{p_s})^2 (1 - 2\overline{p_c})^{2(N_{\text{Cl}}-1)} \text{var}(p_c) \\ &\quad + 2N_{\text{Cl}} (1 - 2\overline{p_s}) (1 - 2\overline{p_c})^{2N_{\text{Cl}}-1} \text{covar}(p_c, p_s). \end{aligned}$$

Here, $\text{covar}(p_c, p_s)$ is the covariance between p_c and p_s , and $\overline{p_c}$ [$\text{var}(p_c)$] and $\overline{p_s}$ [$\text{var}(p_s)$] are the means [variances] of p_c and p_s , respectively.

Measurements of ε_R use $N = 8000$ single-shot measurement outcomes, which we assume are selected from a binomial distribution with mean $(1 - P)$. P is in turn selected from a distribution with mean $\overline{p_e}$ and standard deviation σ_{p_e} . Let N_e be the number of erroneous measurements, given as $N_e = N\varepsilon_R$. In order to calculate the mean and variance in N_e , we have to calculate the first and second moments of the distribution, averaged over all P . We assume a normal

distribution for P . For the first moment we obtain

$$\begin{aligned}\langle N_e \rangle &= \int_{-\infty}^{\infty} \left[\sum_{k=0}^N k \binom{N}{k} P^k (1-P)^{N-k} \right] e^{-\frac{(P-\bar{p}_e)^2}{(2\sigma_{p_e}^2)^2}} \frac{1}{\sqrt{2\pi\sigma_{p_e}^2}} dP \\ &= N \int_{-\infty}^{\infty} P e^{-\frac{(P-\bar{p}_e)^2}{(2\sigma_{p_e}^2)^2}} \frac{1}{\sqrt{2\pi\sigma_{p_e}^2}} dP = N\bar{p}_e.\end{aligned}$$

As expected, the average number of erroneous measurements equals the total number of measurements multiplied by the average error, and is unaffected by fluctuations. For the second moment we calculate

$$\begin{aligned}\langle N_e^2 \rangle &= \int_{-\infty}^{\infty} \left[\sum_{k=0}^N k^2 \binom{N}{k} P^k (1-P)^{N-k} \right] e^{-\frac{(P-\bar{p}_e)^2}{(2\sigma_{p_e}^2)^2}} \frac{1}{\sqrt{2\pi\sigma_{p_e}^2}} dP \\ &= \int_{-\infty}^{\infty} (NP + N(N-1)P^2) e^{-\frac{(P-\bar{p}_e)^2}{(2\sigma_{p_e}^2)^2}} \frac{1}{\sqrt{2\pi\sigma_{p_e}^2}} dP \\ &= N\bar{p}_e + N(N-1)(\bar{p}_e^2 + \sigma_{p_e}^2).\end{aligned}$$

This leads to the final result:

$$\text{var}(\varepsilon_R) = \frac{1}{N} \bar{p}_e (1 - \bar{p}_e) + \frac{N-1}{N} \text{var}(p_e). \quad (\text{S2})$$

The simple model without T_1 fluctuations can be recovered here by setting $\text{var}(p_e) = 0$.

3. Asymmetry

Due to the asymmetry of T_1 , the error rate $p_e^{(j)}$ depends on whether the qubit is in the excited or ground state during τ_{RO} . The measurement, lasting $\tau_m = 1 \mu\text{s}$, is T_1 rather than noise limited. We can approximate it by perfect state update and measurement at $\tau_b \approx 4\tau_m/7 = 0.57 \mu\text{s}$ [S3], followed by a rest time $\tau_a = \tau_{RO} - \tau_b = 3.68 \mu\text{s}$ before the beginning of the next Clifford sequence. Let the system state at the point of the measurement (i.e., τ_b into the measurement time) be $|j\rangle$ with $j = 0$ or 1 . If a single error occurs during the sequence, the flipping sequence will revert the qubit to the same state $|j\rangle$ at the next measurement point. This implies that the process is biased towards states with higher error rate, and so the error rate cannot be simply averaged over that expected individually for $|0\rangle$ and $|1\rangle$. Instead, we let the population fraction of $|j\rangle$ over the experiment be f_j , and solve the steady-state rate equation for f_j :

$$f_j = p_e^{(j)} f_j + (1 - p_e^{(1-j)})(1 - f_j).$$

This leads to an error rate of

$$p_e = \frac{p_e^{(0)}(1 - p_e^{(1)}) + p_e^{(1)}(1 - p_e^{(0)})}{(1 - p_e^{(0)}) + (1 - p_e^{(1)})}. \quad (\text{S3})$$

The error during the RRB sequence is state independent, and so the adjustment to Eq. (S1) comes solely from the adjustment to the SPAM error:

$$p_e^{(j)} = p_s^{(j)} + \frac{1}{2} [1 - (1 - 2p_c)^{N_{Cl}}] (1 - 2p_s^{(j)}),$$

with

$$p_s^{(0)} = p_s^{(c)} + (1 - e^{-\tau_b/T_1}), \quad p_s^{(1)} = p_s^{(c)} + (1 - e^{-\tau_a/T_1}) e^{-\tau_b/T_1}.$$

Here, $p_s^{(c)}$ is a small error accounting for non- T_1 SPAM. Substituting these into Eq. (S3) allows for the calculation of the error p_e as a function of p_c , N_{Cl} , and T_1 . In order to calculate the standard deviation, we must then calculate the first derivative, via

$$\frac{\partial p_e}{\partial T_1} = \sum_j \frac{\partial p_e}{\partial p_e^{(j)}} \left(\frac{\partial p_e^{(j)}}{\partial p_s^{(j)}} \frac{\partial p_s^{(j)}}{\partial T_1} + \frac{\partial p_e^{(j)}}{\partial p_c} \frac{\partial p_c}{\partial T_1} \right). \quad (\text{S4})$$

Here, the value of $\frac{\partial p_c}{\partial T_1}$ is obtained by assuming that p_c can be split into a constant pulse error probability p_{pulse} plus a T_1 -induced error probability $p_c^{(T_1)} = 1 - F_{C1}^{(T_1)}$, with $F_{C1}^{(T_1)}$ as defined in Eq. (3).

B. Measurement of T_1 fluctuations

We perform repeated measurements of T_1 one day after the RRB experiments. We extract T_1 from exponential best fits to standard sliding π -pulse experiments. These measurements rely on qubit initialization by waiting. The benefit of this method is that one can measure T_1 fluctuations independently from fluctuations in residual qubit populations, gate fidelity and readout fidelity (unlike restless sequences). The downside is that one can only probe T_1 in $\Delta t = 2.0$ s intervals. We measure T_1 in $L = 234$ runs l of $M = 21$ measurements each, and calculate the single-sided power spectral density (PSD) as

$$S_{T_1}(f) = \frac{2\Delta t}{LM} \sum_{l=1}^L \left| \sum_{m=1}^M \delta T_{1,l}[m] e^{-i2\pi f m \Delta t} \right|^2,$$

where $\delta T_{1,l}[m] = T_{1,l}[m] - \frac{1}{M} \sum_{m'=1}^M T_{1,l}[m']$. We fit $S_{T_1}(f) = \alpha (f/1 \text{ Hz})^\beta$ to the experimental PSD, finding best-fit parameters $\alpha = 8.4 \cdot 10^{-13} \text{ s}^2/\text{Hz}$ and $\beta = -0.81$ (data and fit are shown in Fig. S2). Extrapolating the PSD to higher frequencies, we can estimate the expected σ_{T_1} in the RRB experiments of Section II by integrating over the frequency interval bounded above by the rate of single RRB experiments ($f_u = 1/0.074 \text{ s}$ at low N_{C1}) and below by the acquisition time for 50 such experiments ($f_l = 1/3.7 \text{ s}$). We find $\overline{T_1} = 21.6 \mu\text{s}$ and

$$\sigma_{T_1} = \left(\int_{f_l}^{f_u} S_{T_1} df \right)^{1/2} = 2.44 \pm 0.1 \mu\text{s}.$$

We estimate the uncertainty in σ_{T_1} by splitting the dataset into 6 subsets of equal length.

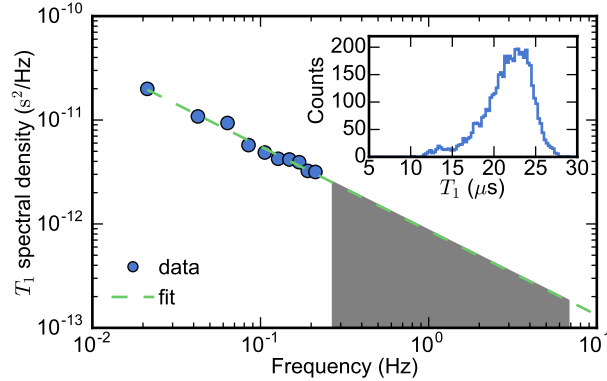


FIG. S2. Power spectral density of T_1 fluctuations. Main panel: measured single-sided PSD of T_1 fluctuations and best fit (see details in text). The indicated frequency range is that relevant for estimating σ_{T_1} in the RRB experiments of Section II. Inset: Histogram of 4914 T_1 measurements. The set has $\overline{T_1} = 21.6 \mu\text{s}$.

C. Relation to experiment

Using the measured $\overline{T_1}$, we fit Eq. (S3) to the data in Fig. 2(a) to extract a common $p_s^{(c)} = 0.006$ and curve specific p_{pulse} . We use Eqs. (S3) and (S4) to obtain the model curves for $\Delta \overline{\varepsilon_R}$ and $\overline{\sigma_{\varepsilon_R}}$ shown in Fig. 3 of the main text, finding good agreement with experiment.

III. GATE SET TOMOGRAPHY AND RANDOMIZED BENCHMARKING FIDELITIES

In order to compare results from GST to those acquired using CRB, the results of GST need to be converted to Clifford fidelities. GST performs a full self-consistent tomography of the gates in the set $\{I, X90, Y90, X180, Y180\}$,

	Conventional	Restless
F_I	0.99928 ± 0.00007	0.99921 ± 0.00005
F_{X90}	0.99927 ± 0.00005	0.99925 ± 0.00004
F_{X180}	0.99920 ± 0.00007	0.99910 ± 0.00005
F_{Y90}	0.99908 ± 0.00005	0.99906 ± 0.00005
F_{Y180}	0.99901 ± 0.00008	0.99891 ± 0.00005
F_{C1}^{GST}	0.99909 ± 0.00005	0.99907 ± 0.00003
F_{C1}	0.9991	0.9991

TABLE S1. Measured gate fidelities in GST. Gate fidelities correspond to average gate fidelities for the four starting conditions of the two-parameter optimization as discussed in the main text.

consisting of the identity and positive $\pi/2$ and π rotations around the x and y axes. The super-operators for the gates in the gate set are extracted from the GST data using pyGSTi [S4]. These are then used to construct the 24 elements ($G_{C1_n}^{\text{GST}}$) of the (single-qubit) Clifford group (\mathcal{G}_{C1}) according to the decomposition of [S5]. To account for the missing negative rotations in the gate set, we replace negative rotations with their positive counterparts (e.g., $-X90 \rightarrow X90$) For each of these operations, the depolarization probability is calculated by looking at the overlap with the target state ($|\rho_t\rangle$) in the super-operator formalism) after applying G_{C1}^{GST} to the input state $|\rho_i\rangle$, for all poles of the Bloch sphere as input states and taking the geometric mean:

$$p_n = \sqrt[n]{\prod_{\rho_i} \langle \rho_t | G_{C1-n}^{\text{GST}} | \rho_i \rangle},$$

where the target state is the state one would get if the gates were perfect:

$$|\rho_t\rangle = G_{C1-n}^{\text{Ideal}} |\rho_i\rangle.$$

p_{C1} is the geometric mean of the individual depolarization probabilities for all $G_{C1_n} \in \mathcal{G}_{C1}$ and related to F_{C1} through $F_{C1} = \frac{1}{2} + \frac{1}{2}p_{C1}$.

Table S1 summarizes the gate fidelities found after performing the two-parameter optimization, for the four starting (A_G , A_D) conditions discussed in the main text.

IV. VERIFICATION OF CONVENTIONAL AND RESTLESS TUNEUP

The speed, robustness and accuracy of the two- and three- parameter optimizations are tested during an 11-hour period by interleaving conventional and restless tuneups with CRB and T_1 experiments. The data summarized in Table 1 of the main text is shown in Fig. S3. The two-parameter (three-parameter) optimization loops over 4 (8) different starting conditions as specified in the main text. The starting condition is updated after each set of conventional and restless optimizations.

-
- [S1] M. A. Rol, C. Dickel, S. Asaad, C. C. Bultink, R. Sagastizabal, N. K. L. Langford, G. de Lange, B. C. S. Dikken, X. Fu, S. R. de Jong, and F. Luthi, “PycQED,” (2016).
[S2] A. Johnson, G. Ungaretti, *et al.*, “QCoDeS,” (2016).
[S3] T. E. O’Brien *et al.*, in preparation (2016).
[S4] E. Nielsen, T. Scholten, K. Rudinger, and J. Gross, “pyGSTi: Version 0.9.1 beta,” (2016).
[S5] J. M. Epstein, A. W. Cross, E. Magesan, and J. M. Gambetta, Phys. Rev. A **89**, 062321 (2014).

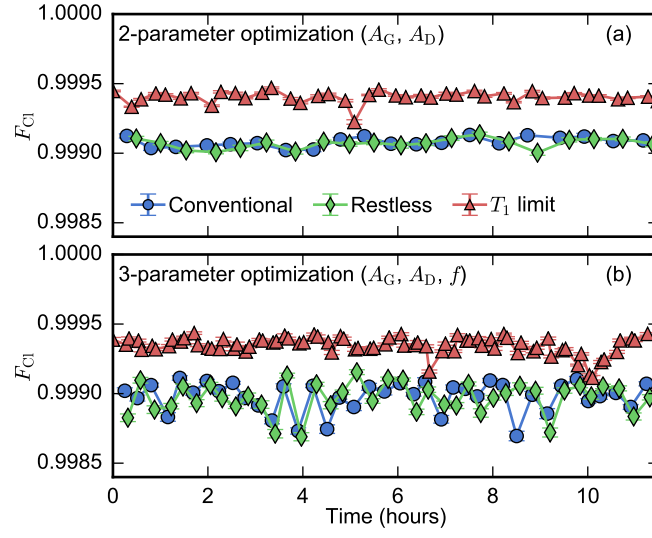


FIG. S3. Performance comparison of repeated restless and conventional tuneups for two parameters (a) and three parameters (b). Each iteration consists of a conventional tuneup followed by a CRB measurement of F_{C1} , a restless tuneup followed by a CRB measurement of F_{C1} , and a T_1 experiment to determine $F_{C1}^{(T_1)}$. For each iteration, a new starting condition is chosen (detailed in main text) that is used for both the conventional and restless tuneup.